Original Research Article: full paper

(2026), "EUREKA: Physics and Engineering" Number 3

IMPLEMENTATION OF ADVANCED TURBULENCE MODELS IN AERODYNAMIC PERFORMANCE PREDICTION OF THE S818-NR AIRFOIL

Muzaffar Hamdamov✉
Department of Mechanics of Fluids, Gas and Drive Systems[1]
mmhamdamov@mail.ru

Khayotjon Aminov
Department of Exact Sciences[2]

Sardorbek Muzaffarov
Department of Mechanics of Fluids, Gas and Drive Systems[1]

Khushvaqt Maratov
Department of Mechanics of Fluids, Gas and Drive Systems[1]

[1]*Institute of Mechanics and Seismic Stability of Structures named after M. T. Urazbaev*
40 Durmon yuli str., Tashkent, Uzbekistan, 100125

[2]*Oriental University*
45 Durmon yuli str., Tashkent, Uzbekistan, 101325

✉**Corresponding author**

Abstract

This research presents a detailed numerical investigation of subsonic airflow around the S818-NR airfoil at angles of attack from 0° to 20°. Using the finite element method in COMSOL Multiphysics, the aerodynamic performance was evaluated, with particular focus on the SST *k-ω* turbulence model, which provided superior accuracy in capturing both near-wall separation and free-stream characteristics. Key parameters, including pressure distributions, velocity components, and lift-to-drag ratios, were analysed across a range of Reynolds numbers ($5 \cdot 10^4$ to 10^6). The computational model was rigorously validated against NASA experimental data, demonstrating high reliability in predicting aerodynamic coefficients. The findings underscore the importance of precise mesh density and solver configurations when simulating modified airfoils such as the S818-NR. These results provide a robust framework for optimising wind turbine blades in low-wind environments, offering a verified numerical approach for developing high-efficiency aerodynamic structures.

Keywords: Navier-Stokes equations, SST model, Comsol Multiphysics, computational experiment, S818-NR, turbulent flow, NASA experimental data.

DOI: 10.21303/2461-4262.2026.004263

1. Introduction

Turbulent flows are among the most challenging phenomena in aerodynamics, characterised by complex, nonlinear interactions that significantly affect the lift, drag, and overall stability of aerodynamic structures. In wind energy, understanding the turbulence around turbine blades is essential for optimising aerodynamic design and improving energy extraction efficiency.

In recent years, rapid advances in computational fluid dynamics (CFD) and increased computing power have transformed the design process for wind turbines and aircraft [1, 2]. Compared with traditional experimental methods, CFD offers a more cost-effective and detailed analysis of flow fields, often serving as the primary means of obtaining high-resolution scientific data in complex fluid dynamics scenarios. Although the aerodynamic performance of various airfoils has been extensively studied, the application of advanced turbulence models to predict the behaviour of modified profiles remains a critical area of investigation.

The aerodynamic performance of S-series airfoils has been a focal point of recent computational studies. For instance, [3] analysed the influence of S809, S811, S814, and S818 geometries

on near-vortex flow zones using ANSYS Fluent. While their findings identified the S818 airfoil as highly efficient, with a superior lift-to-drag ratio and reduced turbulent energy, the research primarily focused on standard profiles and did not consider the geometric modifications required for specific low-wind environments. Similarly, research on flow separation control, such as the implementation of synthetic jet technology on the S809 airfoil [4], demonstrates that while separation can be suppressed, these active control methods add mechanical complexity compared to passive profile optimisation.

Methodological comparisons in the literature further emphasize the importance of turbulence model selection. Investigations into the NREL S809 airfoil [5] using both RNG k-ε and SST k-ω models confirmed that the SST k-ω approach provides superior accuracy in predicting boundary layer behavior. However, as noted in [6], standard RANS-based two-dimensional solvers often exhibit significant discrepancies relative to experimental data in the post-stall region (angles of attack up to 70°). Despite these advancements, a notable research gap remains regarding the modified S818-NR profile. Most existing studies focus on the baseline S818 or S809 geometries, leaving the specific aerodynamic advantages of the 'NR' (Non-Reflective/Modified) variant under-reported, particularly concerning its performance stability across a wide range of Reynolds numbers.

The complexity of airfoil simulations is further highlighted in [7], where steady-state numerical investigations using the EllipSys2D solver showed that computational accuracy is highly sensitive to airfoil geometry and to the precise determination of the laminar-turbulent transition. Furthermore, the transition from two-dimensional to three-dimensional flow dynamics introduces additional variables; for instance, studies of rotating blades based on S809 [8, 9] and NASA series airfoils [10] have identified stall-delay mechanisms driven by Coriolis and centrifugal forces.

While these studies provide a foundational understanding of standard profiles, the modified S818-NR airfoil remains underexplored. Unlike the baseline S818, the S818-NR variant is engineered to enhance lift coefficients and structural integrity for low-wind-speed applications. However, there is a critical lack of comprehensive data on its boundary-layer behaviour and aerodynamic efficiency across varied turbulence models and Reynolds numbers. This research bridges the gap by providing a detailed numerical analysis that offers the necessary insights for the development of high-efficiency wind turbines optimised for low-velocity wind regimes.

The main aim of this work is to investigate the airflow around helicopter and wind turbine blade profiles based on the Reynolds-averaged Navier-Stokes (RANS) equations, as well as to determine the distributed and integral aerodynamic characteristics in the operating range of angles of attack.

2. Materials and methods

From a practical standpoint, airfoils with a relative thickness of 10–18% are of greatest interest, as these profiles are typically found in the midsections of helicopter and wind turbine blades. These sections constitute the majority of the blade's span and largely determine the blade's aerodynamic performance across all flight and operating modes.

The S818-NR airfoil was developed by the US National Renewable Energy Laboratory (NREL) and is intended primarily for use in small- and medium-sized wind turbines. This airfoil is optimized for efficient operation at low and medium wind speeds, ensuring high aerodynamic efficiency and stable power generation under variable wind conditions.

The S818-NR airfoil boasts several key characteristics. Specifically, its maximum relative thickness is approximately 18%, which contributes to high structural strength. This airfoil boasts a high lift coefficient and a low drag coefficient, making it more efficient than other airfoils.

Thanks to its high resistance to flow separation, the airfoil can operate efficiently even at high angles of attack. Furthermore, the S818-NR design accounts for the transition between laminar and turbulent zones, promoting flow stability and efficient energy conversion.

However, in the existing scientific literature, the maximum lift values, flow separation zones, aerodynamic behavior across different Reynolds numbers, and profile stability across different angles of attack have not been studied sufficiently.

In this research, the focus is on numerical modelling of turbulent flow around the S818-NR airfoil. This airfoil is widely used in aerodynamic research due to its simplicity and good lift characteristics. The flow around the airfoil is examined at various angles of attack, ranging from 0 to 20 degrees. For numerical modelling, the Comsol Multiphysics software package is used, which offers extensive capabilities for solving a variety of continuum mechanics problems, including turbulent flow modelling.

Aerodynamic research is a crucial component of wind turbine development and optimization. The S818-NR is one of the most common airfoils. Effective methods such as computational fluid dynamics (CFD) can be used to study the flow around the airfoil and determine its aerodynamic characteristics.

Research using CFD (computational fluid dynamics) methods enables virtual experiments, simulating airflow around an airfoil under various operating conditions. This approach is particularly relevant in wind energy, where airflow is characterized by a wide range of speeds and angles of attack.

Turbulence models and numerical methods are used to estimate aerodynamic parameters. One of the most effective is the Shear Stress Transport (SST) turbulence model, which is used to solve the Navier-Stokes equations that describe the behavior of a viscous fluid or gas. This model accounts for the transition between laminar and turbulent flow regimes and accurately reproduces flow characteristics near the airfoil surface and in regions where flow separation may occur.

The S818-NR turbulent wing profile is designed for operation under virtually incompressible conditions. The Reynolds number per chord is $Re = 10^6$. **Fig. 2** shows the computational grid.

As shown in the airfoil geometry (**Fig. 1**), the S818-NR profile has smooth upper and lower surfaces and moderate camber, which is typical of low-speed aerodynamic applications.

In this research, the commercial software Comsol Multiphysics was used to simulate the flow around a two-dimensional airfoil. The calculations were performed using the Reynolds-averaged unsteady Navier-Stokes (RANS) equations, assuming a steady, incompressible, two-dimensional (2D) flow. These equations form the basis for the mathematical description of incompressible fluid dynamics and represent a system of differential equations that model changes in velocity and pressure in a fluid over time and space.

Since the flow is not completely turbulent, the four-equation SST k-ω turbulent model was chosen to more accurately describe the flow characteristics. A rigid-coupling scheme was used to account for the relationship between pressure and velocity. A second-order discretization scheme was used for the pressure and momentum equations.

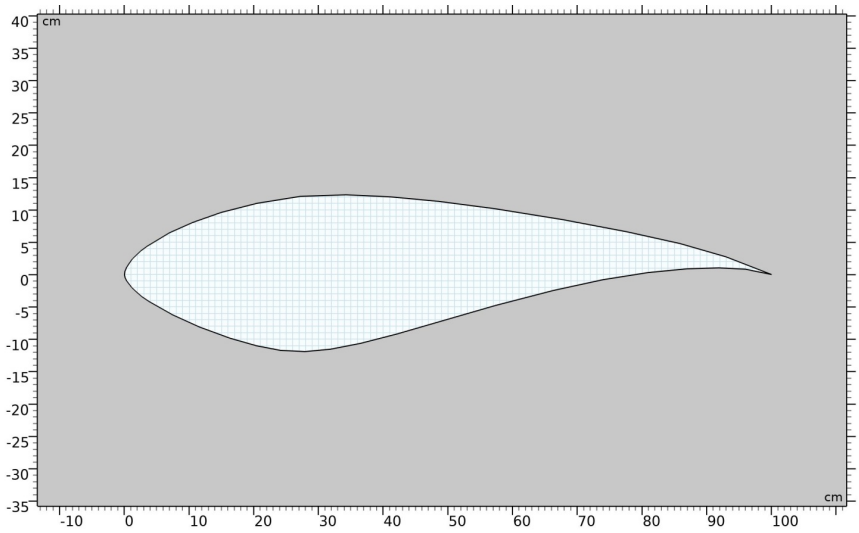
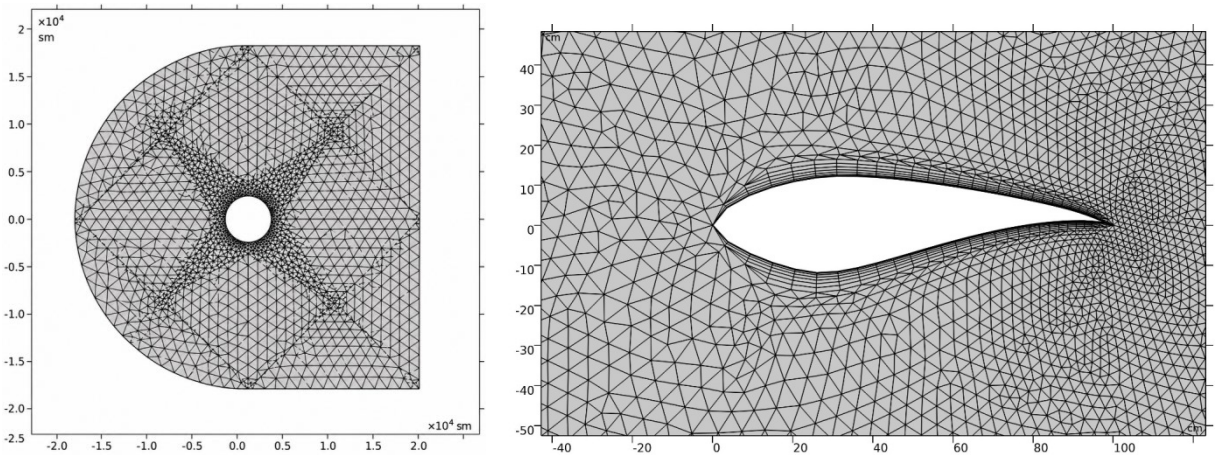


Fig. 1. 2D Profile S818-NR



a *b*

Fig. 2. Computational grid around the aerodynamic profile:
a − overall computational domain; *b* − locally refined grid near the profile

The main equations used in the research are as follows:

1. The continuity equation was calculated using the steady-state approach [11, 12]

$$\frac{\partial\left(\rho U_j\right)}{\partial x_j}=0. \tag{1}$$

2. Time-averaged momentum equation

$$\frac{\partial \rho U_j U_i}{\partial x_j}=-\frac{\partial P}{\partial x_i}+\frac{\partial}{\partial x_j}\left(\mu\frac{\partial U_i}{\partial x_j}\right)+\frac{\partial}{\partial x_j}\left(-\rho\overline{u_i' u_j'}\right). \tag{2}$$

SST model *k*-*ω* Menter (shear stress transport *k*-*ω*) is an improved turbulence model developed by Frank Menter for more accurate calculations of flows with strong pressure gradients, especially near walls and under flow separation conditions. It is widely used in aerodynamics, including modelling the flow around wind turbine blades, wings, diffusers, and other structures.

Menter's SST model *k*-*ω* is a combination of the *k*-*ε* and models *k*-*ω.* The method uses the model *k*-*ω* near the wall, but then (via a special function) switches to *k*-*ε* the – model away from the wall (i.e., closer to the outer edge of the boundary layer).

The equation *k*-*ε* is transformed into the form *k*-*ω* [13].

This allows to take advantage of the advantages of both models:

– the model *k*-*ω* does not require corrections near the wall and more accurately describes flows with an unfavorable pressure gradient. However, the solution depends on the values of turbulent variables in the external flow, especially *ω*;

– the model *k*-*ε* is not as sensitive to these variables, but needs modification near the wall.

It is shown that the Menter SST model *k*-*ω* gives significantly better results in simulating flows with a strong adverse pressure gradient compared to the original models *k*-*ε* and *k*-*ω* [14, 15].

According to [16], this improvement is due to the introduction of the turbulent viscosity limiter proposed by Menter. According to Catalano and Amato [14], compared to other models, Menter's SST model *k*-*ω* is capable of predicting the abrupt flow separation observed in experiments. The results obtained are comparable to those of nonlinear models, but the SST model is less rigid and less computationally intensive.

This model has been successfully applied to numerical simulations of flow around individual wings [17, 18] and to aerodynamic analysis of wind turbines [19].

The model is based on the following two transport equations:

1. Turbulent kinetic energy k

$$\frac{\partial\left(\rho k\right)}{\partial t}+\frac{\partial\left(\rho U_i k\right)}{\partial x_i}=\frac{\partial}{\partial x_j}\left[\left(\mu+\sigma_k\mu_t\right)\frac{\partial k}{\partial x_j}\right]+P_k-\beta^*\rho\omega. \tag{3}$$

2. Specific dispersion ω

$$\frac{\partial(\rho\omega)}{\partial t}+\frac{\partial(\rho U_j\omega)}{\partial x_j}=\frac{\partial}{\partial x_j}\left[(\mu+\sigma_\omega\mu_t)\frac{\partial\omega}{\partial x_j}\right]+\alpha\frac{\omega}{k}P_k-\beta\rho\omega^2+2(1-F_1)\rho\sigma_{\omega2}\frac{1}{\omega}\frac{\partial k}{\partial x_j}\frac{\partial\omega}{\partial x_j}. \quad (4)$$

To determine the turbulent viscosity in the SST k-ω model, the following formula is used

$$\mu_t=\frac{\rho k}{\omega}\frac{1}{\max\left(1,\frac{\alpha^*\omega}{SF_2}\right)}. \quad (5)$$

The coefficient P_k indicates the rate at which turbulent energy k is generated in the flow as a result of velocity shear or flow deformation

$$P_k=\mu_t\left(\frac{\partial U_i}{\partial x_j}+\frac{\partial U_j}{\partial x_i}\right)\frac{\partial U_i}{\partial x_j}. \quad (6)$$

SST k-ω model uses two key switching functions, F_1 and F_2, which determine which turbulence model is applied in different flow zones.

F_1 – active in near-wall regions and ensures model utilization k-ω near the wall. This feature is especially important for accurate modeling of laminar-turbulent transitions and shear layers, where k-ω the model yields more accurate results

$$F_1=\tanh\left(\left[\min\left(\max\left(\frac{\sqrt{k}}{\beta^*\omega y},\frac{500\nu}{y^2\omega}\right),\frac{4\rho\sigma_{\omega2}k}{CD_{k\omega}y^2}\right)\right]\right). \quad (7)$$

F_2 – begins to dominate in zones far from the wall, facilitating a smooth transition to the model k-ε. This is important in free-flow zones, where k-ε the model does a better job of describing turbulence

$$F_2=\tanh\left(\left[\max\left(\frac{2\sqrt{k}}{\beta^*\omega y},\frac{500\nu}{y^2\omega}\right)\right]\right). \quad (8)$$

In (7), (8) ρ – the density; U – the velocity vector; μ – the molecular (dynamic) viscosity; μ_t – the turbulent viscosity; P_k – the source of turbulent kinetic energy, y – the distance to the nearest wall; (m), α, β, β^*, σ_k, σ_ω, $\sigma_{\omega2}$ – model constants; $CD_{k\text{-}\omega}$ – modified diffusion term

$$CD_{k\omega}=\max\left(\frac{2\rho\sigma_{\omega2}}{\omega}\nabla k\cdot\nabla\omega,10^{-10}\right),$$

where $\nabla k\cdot\nabla\omega$ – the scalar product of the gradients k and ω.

Closing the system requires the use of the perfect gas equation of state

$$p=\rho RT, \quad (9)$$

where R is the reduced gas state of air; T = 293.15 K – air temperature.

For the considered variants of the problem, the Reynolds number was [20]

$$\mathrm{Re}=\frac{\rho u_0 l}{\mu}=\frac{1.2043\times20\times1}{1.81397\times10^{-5}}=1.327805\times10^6,$$

which corresponds to a developed regime of turbulent flow around a solid surface. That is, in the calculations, μ = 1.81397 · 10^{-5} kg/m·s and turbulence model is selected accordingly.

The use of Reynolds-averaged Navier-Stokes equations allows for the consideration of turbulent effects and their impact on the flow around the S818-NR airfoil. These equations are solved numerically, such as by finite element analysis, using specialized software packages such as Comsol Multiphysics. This approach provides detailed data on the flow characteristics and their impact on the airfoil.

SST turbulence model the objective of this paper is to simulate turbulent flow problems around the S818-NR airfoil. The obtained numerical data are compared with known experimental data available on the NASA turbulence modelling resource (TMR) website [1, 3].

Boundary conditions on the semicircle and on the boundaries $y = \pm 20$ m (on the boundary G_1, **Fig. 2**) are set depending on the angle of attack

$$U\left(x_{G_1}, y_{G_1}\right) = U_0 \cos\alpha,\ V\left(x_{G_1}, y_{G_1}\right) = U_0 \sin\alpha, \tag{10}$$

where U_0 – the modulus of the velocity of the flow incident on the main undirected stream; α – the angle between the direction of flow and the coordinate axis OX.

At this boundary, the excess pressure value is zero

$$p\left(x_{G_1}, y_{G_1}\right) = 0 \text{ Pa}. \tag{11}$$

Accordingly, for the border

$$G_2 = \left(0 \le x \le 1\right) \cap \left(y = f_1\left(x\right) \cup f_2\left(x\right)\right),$$

set the conditions $U(x_{G2}, y_{G2}) = U(x_{G2}, y_{G2}) = 0$ m/s.

At the exit from the calculation region, $y = 2$ m (G_3), the condition G_3 of smooth conjugation was adopted to determine the velocities:

$$\frac{\partial U\left(x_{G_3}, y_{G_3}\right)}{\partial n} = 0,$$
$$\frac{\partial V\left(x_{G_3}, y_{G_3}\right)}{\partial n} = 0. \tag{12}$$

For the standard turbulence model *SST* Standard Comsol Multiphysics solvers were used. Calculations were carried out for $50000 < \text{Re} < 1000000$ for different angle of attack options from the interval $0 \le \varphi \le 20°$.

In the calculations, local grid thickening was used near the surface of the profile $f_1(x)$ and $f_2(x)$ shown in **Fig. 1**.

50600 elements were used for the airfoil flow region. To ensure stable convergence of the calculations, the convergence criteria were set to 10^{-6}.

To solve the problem, the steady-state method was used. Potential flow results were applied as an initial approximation. The program's operation on finite volumes is based on first determining velocity fields for a fixed time. These fields are used to determine the pressure increments, relative to which Poisson's equation is derived.

On average, the program ran for two or more hours. The outputs included longitudinal and transverse velocity fields, pressure fields, turbulent kinematic energy and its dissipation, and aerodynamic derivatives.

The raw data obtained from the Comsol Multiphysics simulations, including pressure distribution and wall shear stress, were processed to determine the integral aerodynamic characteristics. The lift (C_l) and drag (C_d) coefficients were calculated by integrating the local pressure p and skin friction (τ_w) forces over the airfoil surface S using the following expressions:

$$C_l = \frac{1}{\frac{1}{2}\rho \vartheta^2 c} \oint \left(p \cdot n \cdot j + \tau_w \cdot t \cdot j\right) \mathrm{d}s,$$

$$C_d = \frac{1}{\frac{1}{2}\rho \vartheta^2 c} \oint \left(p \cdot n \cdot i + \tau_w \cdot t \cdot i \right) \mathrm{d}s, \tag{13}$$

where c – the chord length, n and t – the normal and tangential unit vectors, i and j – the unit vectors in the lift and drag directions.

The integration was performed using Comsol's built-in boundary integration tools with a high-order quadrature method to ensure numerical precision. The pressure distribution results were also compared with the coordinates provided by the Airfoil Tools database to ensure geometric consistency during the post-processing phase.

To ensure the reliability of the numerical results, the current computational model was validated against experimental data for the S818-NR airfoil. The experimental data were obtained from the NASA [21], which provides high-fidelity wind tunnel test results. The validation was conducted at a Reynolds number of Re = 10^6. A comparison was made between the calculated lift (C_l) and drag (C_d) coefficients and the NASA experimental values across various angles of attack. The high degree of correlation between the numerical simulations and the experimental measurements confirms the validity of the chosen mesh density and the SST turbulence model settings used in this research.

3. Results and discussion

The pressure coefficient (or relative pressure coefficient) is a dimensionless quantity that shows the ratio of the difference between the local pressure on the surface of a body and the pressure of the incoming flow to the dynamic pressure of the flow.

The change in excess pressure along the channel wall depending on the distance to the top is called the distribution of the surface pressure coefficient [22, 23]

$$C_p = \frac{p - p_\infty}{0.5 \rho U_0^2}, \tag{14}$$

where p – the pressure at a point on the profile surface; p_∞ − free flow pressure; ρ − free flow density; U_0 − free flow velocity.

Comparisons of the obtained numerical results with known experimental data are shown below. **Fig. 3** shows the pressure coefficients for various angles of attack of the airfoil surface.

Dependence of the pressure coefficient C_p The angle-of-attack relationship is an important tool for analyzing and optimizing airfoils. It allows one to evaluate airfoil performance under various conditions and use this information to design more efficient aerodynamic shapes.

In the region of the leading edge ($x \approx 0$–5 mm), a sharp drop in the pressure coefficient C_p is observed. This indicates an acceleration of the airflow along the upper surface of the airfoil, causing a significant decrease in static pressure. As a result, a strong vacuum zone develops on the upper surface, causing the generation of a strong lift force.

In the upper surface region (5 mm < x < 70 mm), the pressure coefficient remains strongly negative but gradually increases, indicating partial pressure recovery. However, the low-pressure zone remains wide, indicating a strong aerodynamic force and simultaneously increasing the risk of flow separation. The slow pressure recovery may be due to a decrease in the pressure gradient, which makes it difficult for the inertial flow to remain on the airfoil surface.

On the lower surface, on the other hand, the pressure is relatively higher (in some places, the pressure coefficient even reaches positive values), indicating a slower airflow and, consequently, higher pressure. The significant pressure difference between the upper and lower surfaces of the airfoil results in significant lift.

At the rear of the airfoil ($x \approx 90$ – 100 mm), the C_p values on the upper and lower surfaces approach each other but do not completely equalize. This indicates that the airflow around the airfoil is not fully restored, and residual vortex phenomena and energy losses in the flow are possible.

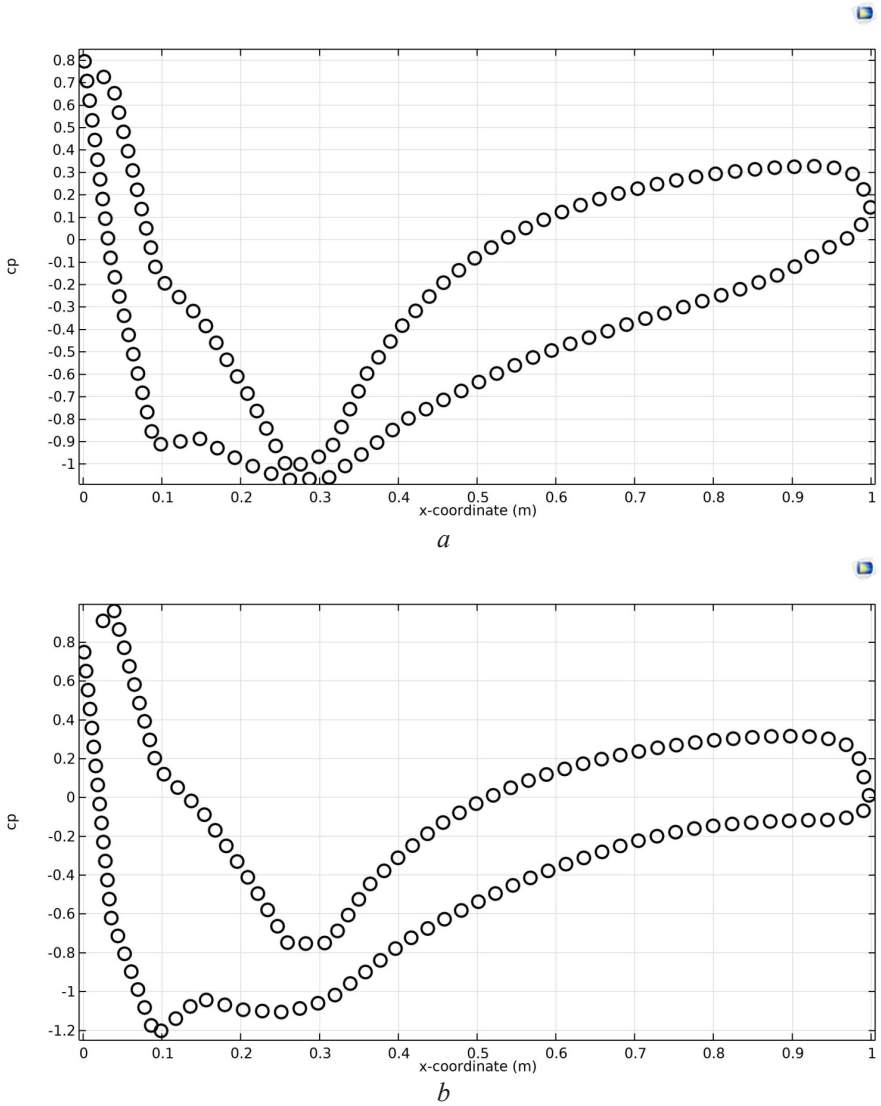


Fig. 3. Shows the pressure coefficients for various angles of attack of the airfoil surface: *a* − distribution of the surface pressure coefficient C_p at $\alpha = 5°$ angle of attack; *b* − distribution of the surface pressure coefficient C_p at $\alpha = 10°$ angle of attack

Analyzing the flow velocity contours around an airfoil at different angles of attack helps understand how the velocity distribution changes and where high- and low-velocity zones arise. This is important for assessing the airfoil's efficiency and identifying areas of potential flow separation.

Fig. 4 shows the longitudinal velocity field around an airfoil. Each subfigure represents the airflow velocity distribution at different angles of attack (α). Blue indicates low-velocity zones (or stagnation regions). Red corresponds to high flow velocities. Green and yellow represent intermediate values. The color scale is located to the right of the graph.

At low angles of attack ($\alpha = 2°, 4°$), the flow around the airfoil is smooth, with virtually no separation. The flow continues behind the airfoil, indicating a laminar flow. Lift is present, and the airfoil's efficiency is high.

At moderate angles of attack (e.g., $\alpha = 8°, 10°, 12°$), a decrease in pressure is observed on the upper surface of the airfoil (on the back), with red areas predominating. Flow separation begins, which is especially noticeable at $\alpha = 12°$. These angles approach the maximum lift value.

At high angles of attack ($\alpha = 14°, 16°, 20°$), the flow separation zone (especially the reverse flow – blue) increases significantly. A separation zone is clearly visible behind the airfoil. In this mode, drag increases and lift decreases, leading to a stall.

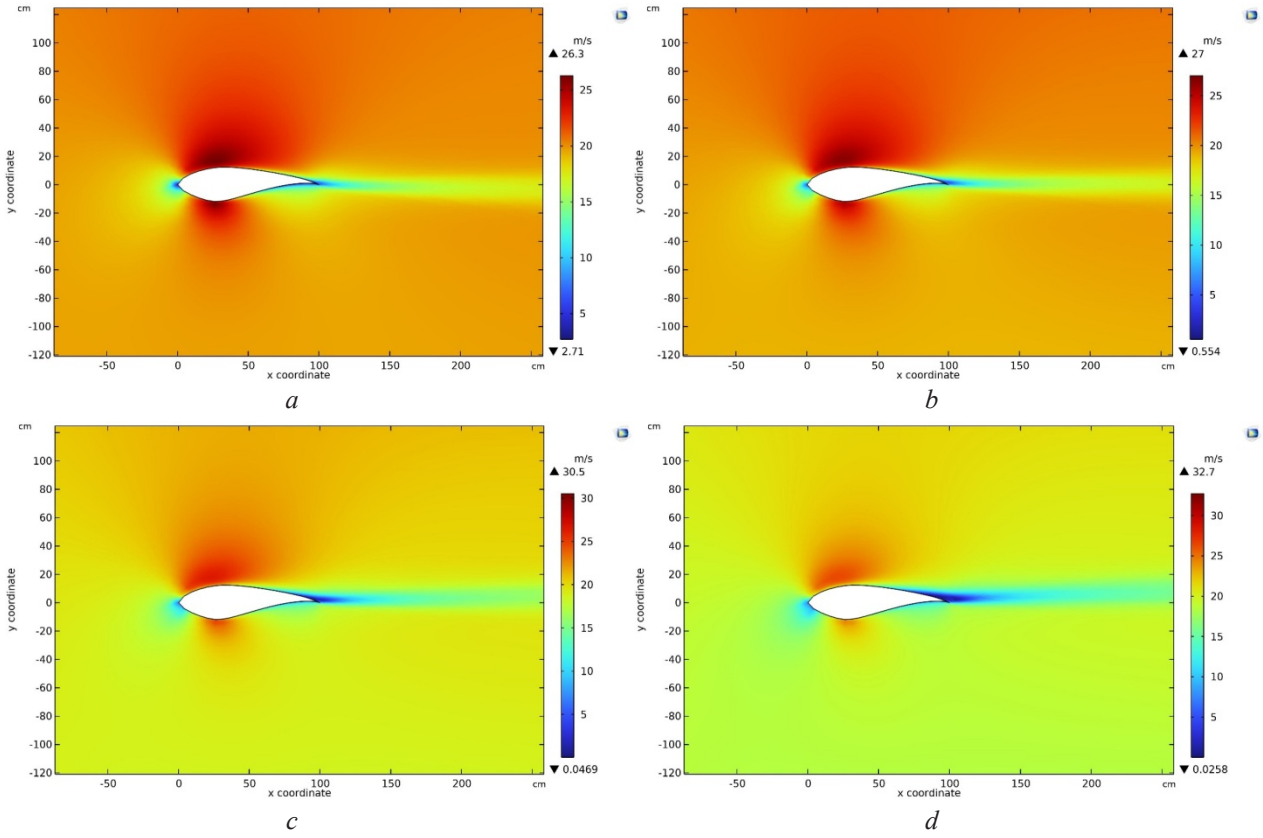


Fig. 4. Longitudinal velocity field: *a* – α = 4°; *b* – α = 10°; *c* – α = 16°; *d* – α = 20° angle of attack

Overall, the range α = 8–12° is most efficient for the profile. As α > 12°, separation increases and efficiency drops sharply. At α = 20°, a large stagnation zone is observed behind the profile, indicating a complete flow stall.

In the region near the airfoil's leading edge, particularly near the upper surface, a zone of high positive transverse (*y*) velocity is observed (**Fig. 5**), shown as red-green colouration on the flow map. This indicates accelerated upward motion of the air mass along the airfoil's upper surface. In this region, an intense pressure drop occurs, forming a rarefaction zone that contributes to the generation of significant lift.

At the upper surface of the profile, the flow is deflected upwards in the y-direction, indicating contact with the surface. The colour range varies from green to yellow and red, indicating a high *y*-component of the velocity. This, in turn, corresponds to a region of increased flow velocity and reduced pressure.

Blue zones are visible on the lower surface of the airfoil, indicating a downward transverse flow. Here, the flow is relatively slower, and the *y* – component of the velocity is negative and small. This indicates a region of higher pressure beneath the airfoil.

The flow over the upper and lower surfaces moves in opposite directions and does not fully level off towards the trailing edge. This indicates that the flow has not yet been fully restored, and there may be separation zones or low flow energy.

The pressure isolines are shown in **Fig. 6** below.

Plotting pressure field isolines at different angles of attack is an important part of aerodynamic analysis, as it allows one to visualize the pressure distribution around an airfoil and evaluate its characteristics. Based on the obtained pressure isolines (**Fig. 7**) An analysis of the pressure distribution on the aerodynamic profile at different angles of attack was carried out.

A numerical study of the pressure distribution and flow structure on an airfoil at various angles of attack revealed consistent changes in its behaviour. At small angles (α = 2°), the flow is stable and lift is low. As the angle of attack increases to α = 8–12°, the rarefaction zone on the upper

surface intensifies, the pressure drop increases, and the lift coefficient (C_L) reaches its maximum, corresponding to the airfoil's highest aerodynamic efficiency. With a further increase in the angle of attack (α = 14–16°), flow separation begins: the separation zone gradually expands, leading to a decrease in efficiency. At α = 20°, complete flow separation occurs, accompanied by a sharp drop in lift and an increase in drag (C_D), which significantly degrades the airfoil's aerodynamic performance.

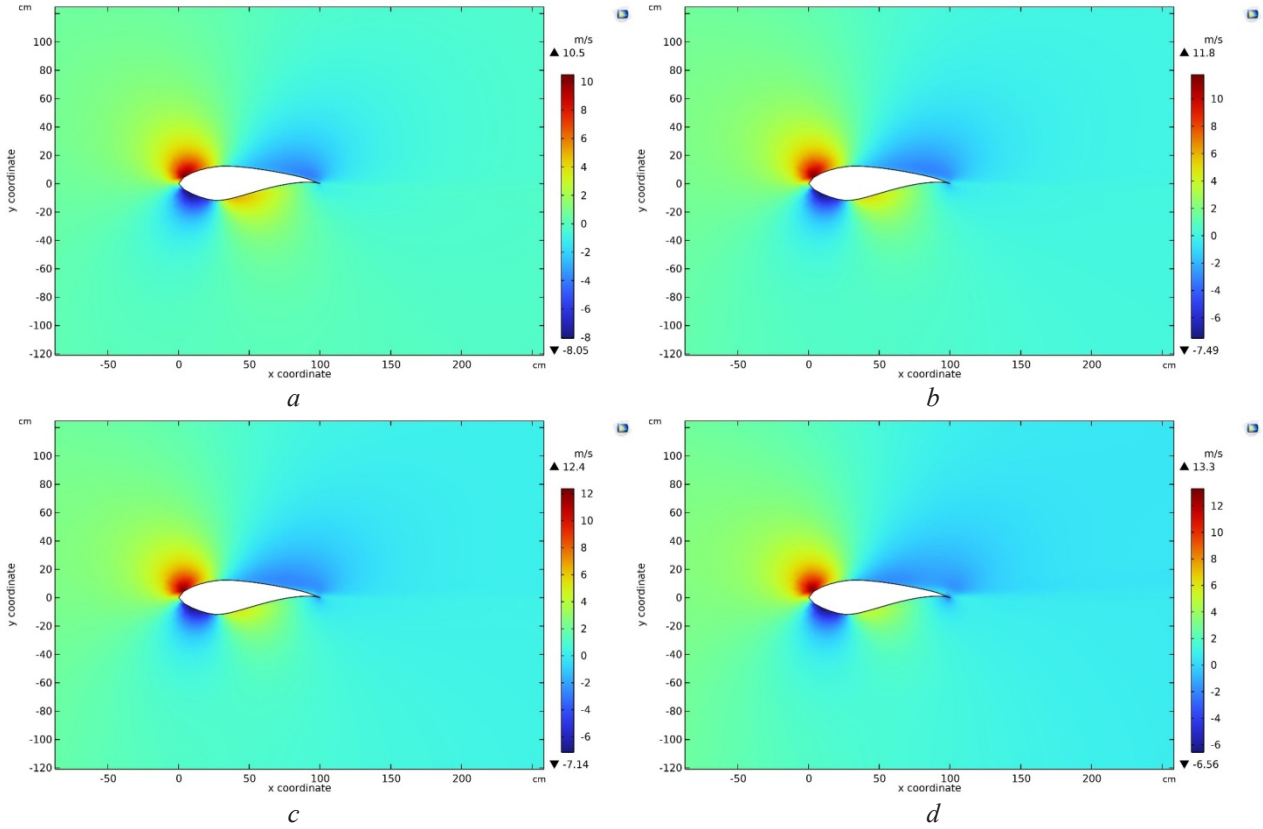


Fig. 5. Field of transverse velocity: *a* – α = 2°; *b* – α = 10°; *c* – α = 14°; *d* – α = 20°

For this profile, the optimal angle of attack is approximately α = 10°~12°. At angles α > 14°, the flow separation zone expands, leading to a reduction in lift and a deterioration in aerodynamic efficiency. The analysis performed allows to clearly determine the nature of the lift and drag force changes and establish the flow stability boundary around the airfoil.

Analysis of the isolines of the kinetic energy of the turbulent flow (**Fig. 7**) around the airfoil at different angles of attack helps to visualize this, which is important for assessing the efficiency of the airfoil and understanding the turbulent characteristics of the flow.

Turbulent kinetic energy (TKE) is an important metric for assessing flow instability, the presence of separation zones, and their impact on aerodynamic efficiency. Below is an analysis of the TKE distribution at various angles of attack α.

A numerical study of the distribution of turbulent energy at different angles of attack showed a consistent change in the flow characteristics. At α = 2° the flow is close to a laminar regime, the separation zone is practically absent, which corresponds to a stable state. With an increase in the angle to α = 6° the growth of turbulent energy behind the profile and the formation of a separation zone begins. At α = 8° Turbulence increases significantly, the plume zone becomes less stable, which leads to aerodynamic losses. At α = 10° a partial restoration of flow stability is observed: the lift force remains high, and the level of turbulent energy decreases – this regime can be considered close to optimal. A further increase in the angle (α = 14°) is accompanied by the development of pronounced separation, which reduces efficiency. At α = 20° a complete flow separation is recorded: the separation zone is stable and large, the lift force drops sharply, and the resistance increases significantly.

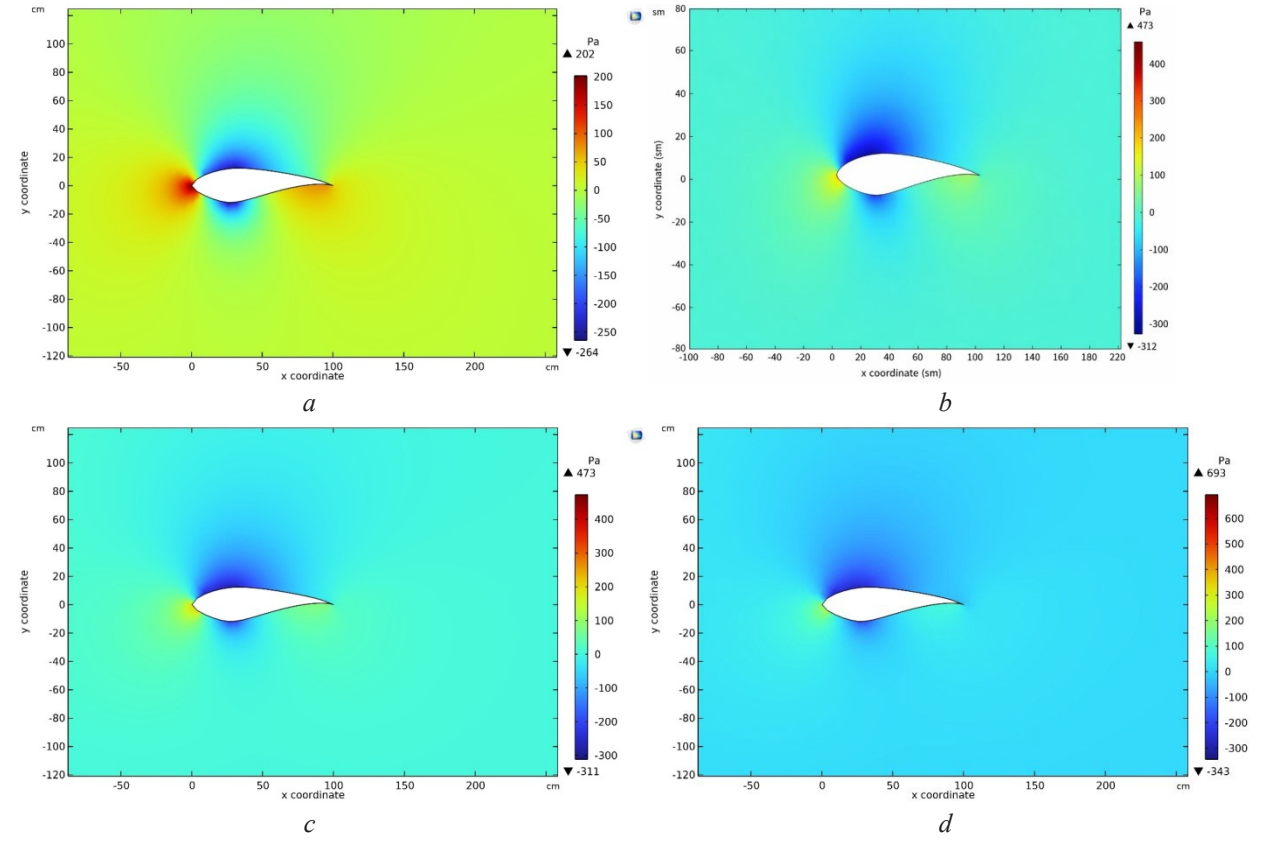


Fig. 6. Pressure field isolines: *a* – $\alpha = 2°$; *b* – $\alpha = 6°$; *c* – $\alpha = 14°$; *d* – $\alpha = 20°$

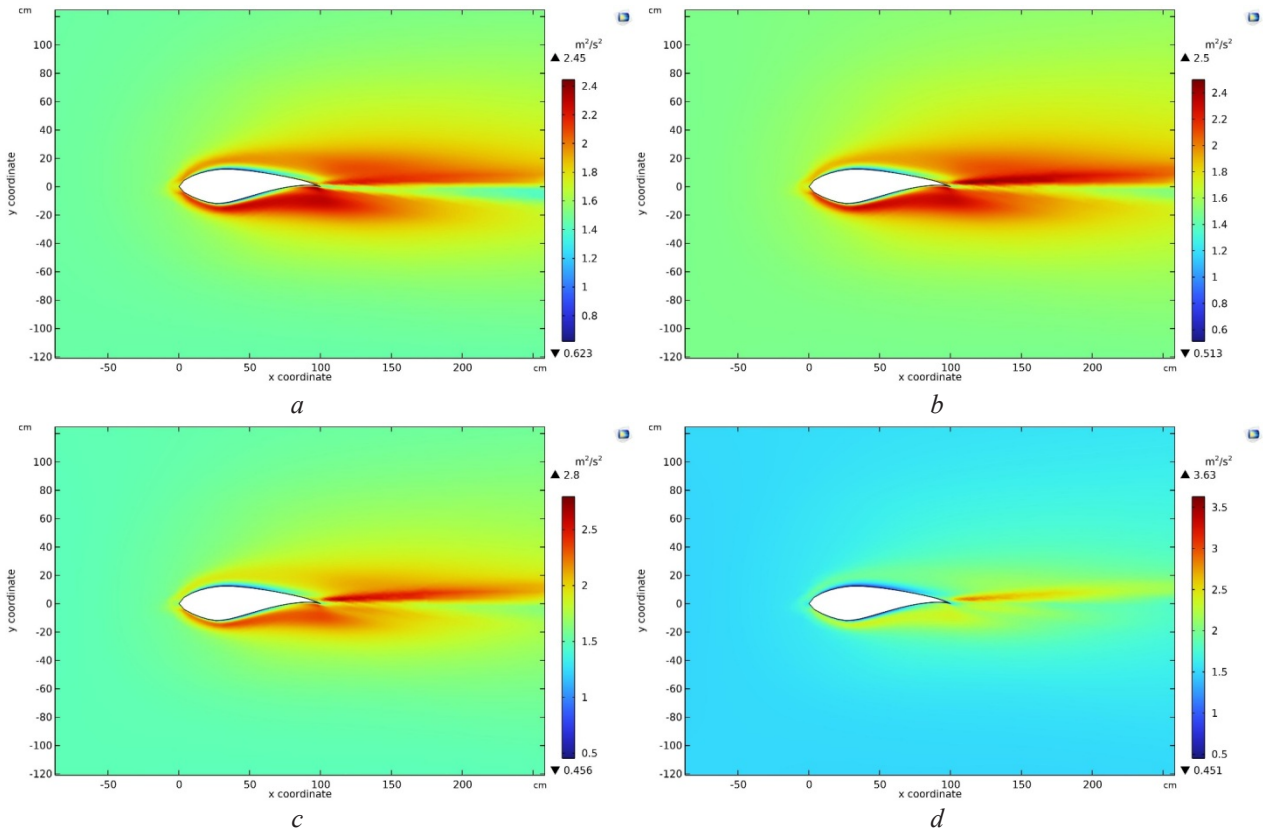


Fig. 7. Isolines of flow turbulence kinetic energy: *a* – $\alpha = 2°$; *b* – $\alpha = 6°$; *c* – $\alpha = 8°$; *d* – $\alpha = 10°$

Analysis showed that the optimal aerodynamic regime for turbulence kinetic energy is observed in the range $\alpha = 6°\sim10°$. At $\alpha > 14°$, the flow becomes unstable, aerodynamic efficiency decreases, and separation zones expand. This assessment provides an important basis for flow control, early detection, and reduction of aerodynamic losses.

Fig. 8 shows the pressure coefficient fields C_p around an aerodynamic profile at different angles of attack α. The pressure coefficient C_p reflects the ratio of local pressure to dynamic pressure and plays a key role in determining lift and flow stability.

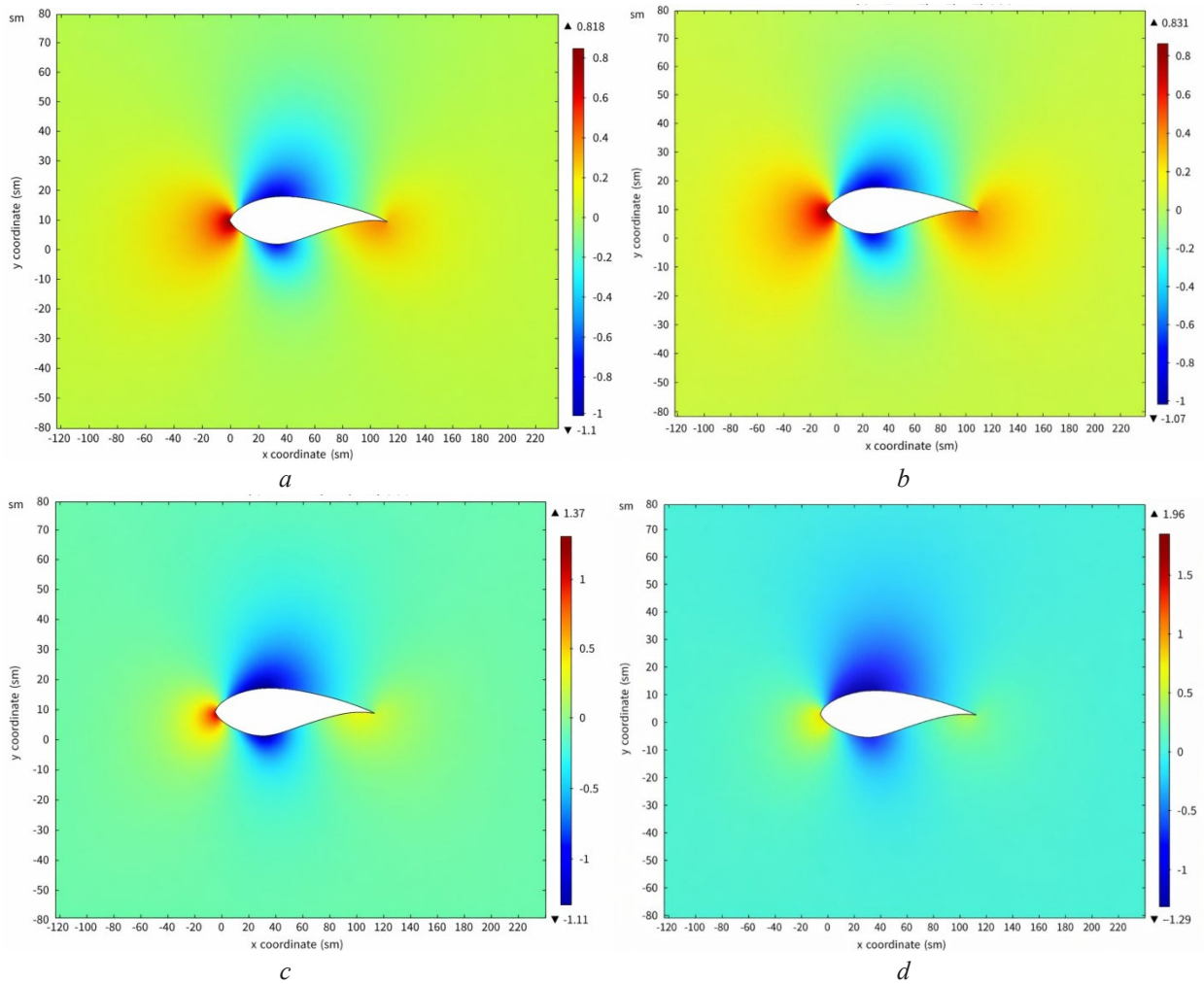


Fig. 8. Isolines of C_p distribution: a – $\alpha = 2°$; b – $\alpha = 6°$; c – $\alpha = 10°$; d – $\alpha = 14°$

The optimal range of angles of attack for this profile is $\alpha = 6°\sim10°$. At $\alpha > 14°$ the onset and development of flow separation is observed, which leads to a decrease in lift and an increase in drag.

When studying the aerodynamic characteristics of airfoils (wings), the key quantities are lift (L) and its relative coefficient (C_L). These parameters play a crucial role in assessing the airfoil's effectiveness when interacting with the airflow.

Investigating how airfoil geometry affects lift is an integral part of aerodynamic analysis. Different airfoil shapes – for example, S818, NACA 4412, and NACA 0012 – produce different lift coefficients under identical conditions, making airfoil selection a critical design step.

It's worth noting that studying an airfoil without taking lift into account is like studying a bird without wings. To understand why an airfoil has a particular shape, it's first necessary to determine how much lift it can generate when interacting with the airflow [24, 25]

$$C_L = \frac{L}{0.5\rho V^2 S}, \tag{15}$$

where C_L – the lift coefficient (dimensionless value); L – the lift force (Newtons, N); ρ – the air density (kg/m^3); V – the air flow velocity (m/s); S – the wing (profile) projection area (m^2).

Fig. 9 analyzes the dependence of the lift coefficient C_L on the angle of attack.

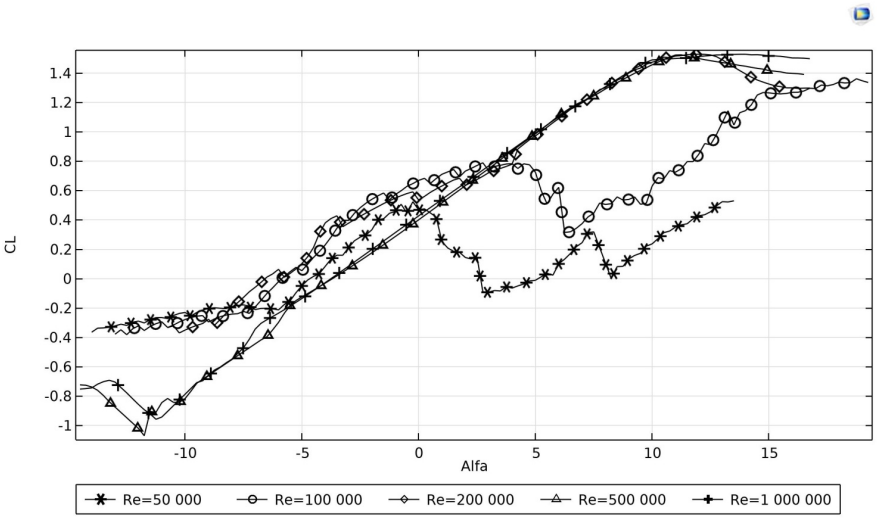


Fig. 9. Analysis of the dependence of the lift coefficient C_L on the angle of attack

The following patterns are observed from the graph.

For all *Re* values, an increase in C_L *is* observed with increasing angle of attack to approximately 10–12°, and at Re = 500000 and Re = 1000000 the increase occurs smoothly and steadily, reaching a maximum value of $C_L \approx 1.4$. After reaching the maximum, flow separation occurs, during which C_L drops sharply. At low Re, for example at Re = 50000, separation occurs early – already around 6°. At Re = 100000 and 200000, the separation is more pronounced. At high Re (500000 and 1000000), the drop in C_L is less sharp, indicating high aerodynamic stability of the profile.

At negative angles of attack ($\alpha < 0$), C_L takes on negative values, indicating the generation of downward lift. In this range, C_L behavior also depends on the Reynolds number: at high Re values, the airfoil copes better with laminar flow separation. Thus, at high Reynolds numbers (Re ≥ 500000), the S818-NR airfoil demonstrates high aerodynamic efficiency: significant C_L values, smooth flow separation, and stable lift growth. At the same time, at low Re (≤ 100000), early laminar separation limits the growth of C_L and reduces airfoil efficiency.

For the S818 airfoil, at a calculated Reynolds number $2.5 \cdot 10^6$, the maximum lift coefficient is 1.68. These performance characteristics are particularly important when selecting an airfoil for both low-speed and high-speed installations such as wind turbines or large unmanned aerial vehicles.

The drag coefficient (C_D) is also a key parameter when evaluating an airfoil's aerodynamic performance. This coefficient reflects the degree of resistance of the airfoil to airflow. Combined with the lift coefficient (C_L), the coefficient C_D plays a key role in analyzing the airfoil's overall aerodynamic efficiency. The ratio C_L/C_D is particularly important; its maximum value serves as a criterion for determining the optimal operating mode.

The drag coefficient C_D is a dimensionless value that characterizes the ability of a body (e.g., an airfoil, wing, or body) to resist air movement. It is determined by the formula [20]

$$C_D = \frac{D}{0.5\rho V^2 S}, \tag{16}$$

where C_D – the drag coefficient (dimensionless value); D – the aerodynamic drag force (N); V – the air flow velocity (m/s), S – the wing projection area (profile) (m^2).

Fig. 10 presents the dependence of the drag coefficient C_D on the angle of attack at different Reynolds numbers.

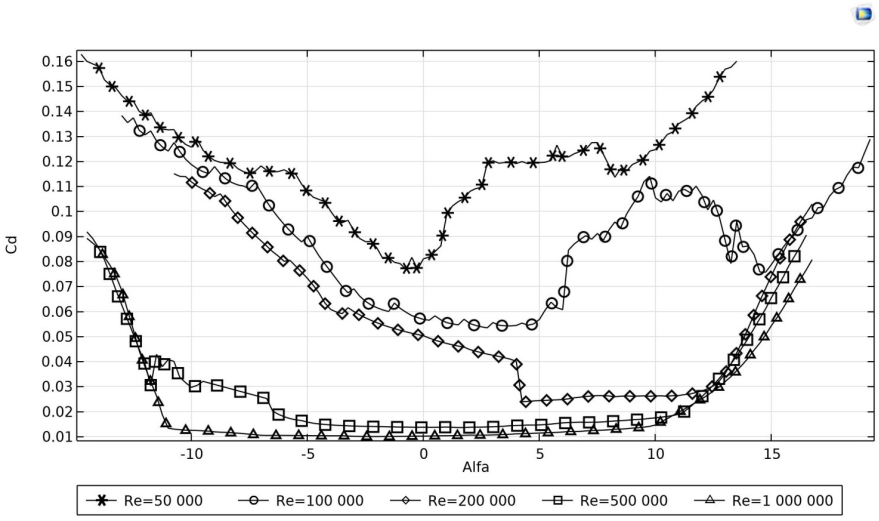


Fig. 10. Analysis of the dependence of the angle of attack on the drag coefficient (C_D) at different Reynolds numbers

Below is an analysis of the dependence of the drag coefficient C_D of the S818-NR aerodynamic profile on the angle of attack α at different Reynolds numbers (Re).

In this range Re = 50000 – 100000, the C_D values are relatively high, especially in the range of 0–6°. This is due to early laminar flow separation, during which the flow around the airfoil becomes unstable and separation zones form in the upper layer. As the angle of attack increases, the drag coefficient C_D increases, reducing the overall aerodynamic efficiency of the airfoil. As the stall angle approaches – approximately 6–8° C_D increases sharply due to complete flow separation and the development of pronounced turbulence.

In the range of Re = 200000–500000, the initial values of C_D are significantly lower, indicating stable and smooth flow around the airfoil surface. As the angle of attack increases, C_D increases, but no sharp jumps are observed until the flow stalls. Particularly noteworthy is the behavior at Re = 500000, where C_D is only slightly sensitive to changes in the angle of attack, and the airfoil maintains high stability and aerodynamic efficiency.

At Re ≥ 1000000, the lowest initial values of C_D are observed, since the flow is entirely near-wall and laminar separation is absent. As the angle of attack increases, C_D increases very slowly, and even when stall occurs, there is no sharp jump in C_D, indicating high stability and flow quality.

As the Reynolds number increases, the C_D coefficient decreases, indicating improved wall flow and reduced drag. At low Re, laminar separation occurs earlier, increasing the C_D and degrading aerodynamic performance. At high Re (≥ 500000), the airfoil exhibits low drag, stable behavior, and delayed flow separation, making it particularly suitable for wind energy and aircraft applications.

The lift coefficient C_L (**Fig. 11**) calculated data according to the SST k-ω model are in good agreement with the results of experimental measurements. The maximum value of C_L is achieved at an angle of attack of $\alpha \approx 10$–12° (approximately 1.2–1.25). With a further increase in the angle of attack, a drop in C_L is observed, which indicates flow separation. Overall, the model slightly overestimates the C_L values compared to experiment, but the deviations are within acceptable limits.

Resistance coefficient C_D (**Fig. 12**) increases smoothly with increasing angle of attack. Up to $\alpha \approx 12$–14° the results of the model and experiment practically coincide. At $\alpha > 14°$ a noticeable increase in C_D is observed, especially after 16°, which is associated with an increase in the flow separation zone and an increase in turbulence. The SST k-ω model slightly overestimates the C_D values at large angles, which is typical for numerical simulations with high sensitivity to flow separation.

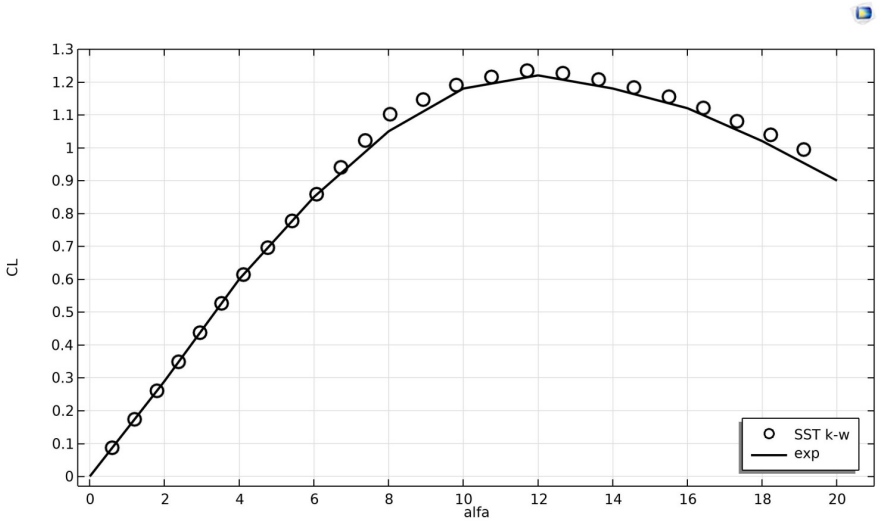


Fig. 11. Experimentally and theoretically determined lift coefficients [21]

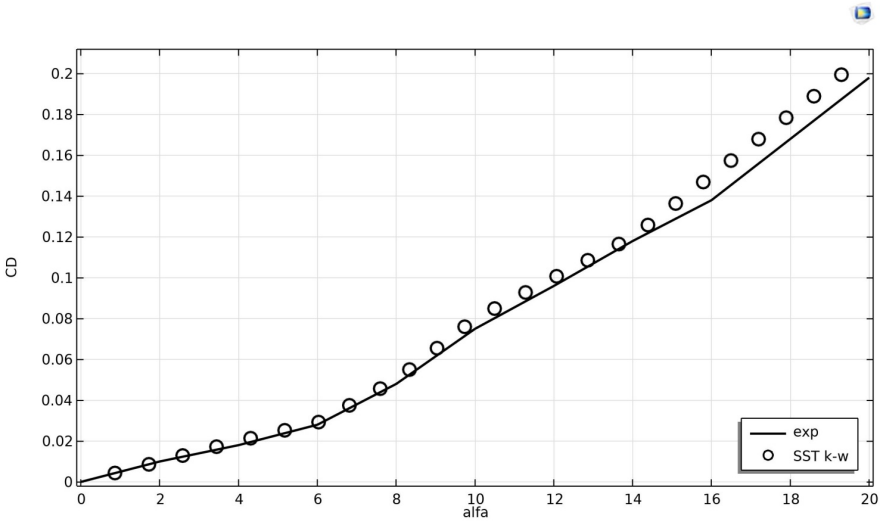


Fig. 12. Comparison of the drag coefficient with experimental data [21]

The moment coefficient C_m is a dimensionless parameter characterizing the aerodynamic torque generated around a specific point on the airfoil, typically a quarter-chord. C_m reflects the extent to which aerodynamic forces tend to rotate the airfoil around the center of rotation. This coefficient is key in assessing static stability and controllability. And profile sensitivity to flow separation. It is determined by the formula [26, 27]

$$C_m = \frac{M}{0.5\rho V^2 cS}, \tag{17}$$

where M – the aerodynamic moment (N m); ρ – the air density (kg/m^3); V – the flow velocity (m/s); c – the profile chord length (m); S – the wing or profile area (m^2).

At $C_m < 0$, the airfoil exhibits static stability, meaning the torque tends to return it to its original position as the angle of attack increases. At $C_m > 0$, static instability is observed, which can cause control difficulties. The point at which $C_m = 0$ corresponds to neutral stability there is no torque.

Fig. 13 analyzes the aerodynamic behavior of the S818 airfoil at different Reynolds numbers, in particular the dependence of the moment coefficient C_m on the angle of attack α. The graph was used to determine the airfoil stability, the onset of flow separation, and the overall efficiency level.

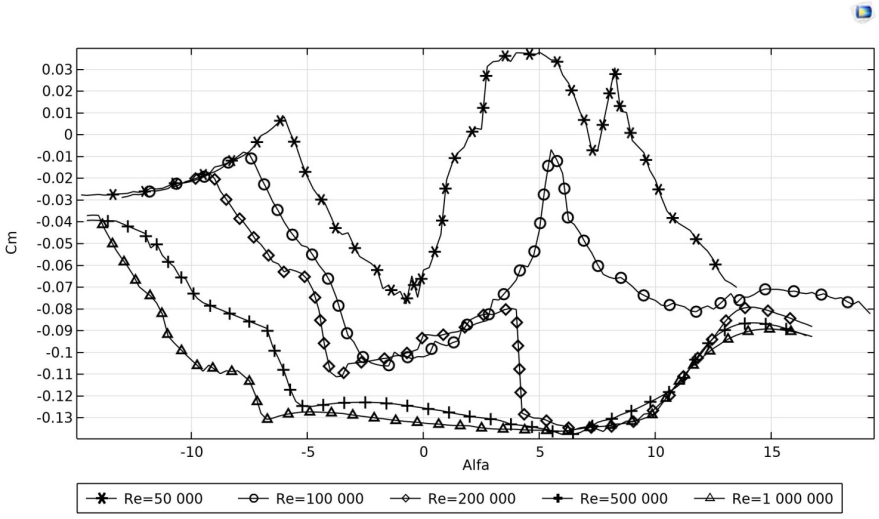


Fig. 13. Change in the coefficient of moment C_m depending on the angle of attack α for different values of the Reynolds number

It was found that with increasing Reynolds number, the C_m curve becomes smoother, and the overall stability of the airfoil increases. Specifically, at Re = 50000 and Re = 100000, sharp fluctuations in the C_m curve are observed, indicating laminar flow separation and aerodynamic instability at low speeds.

Starting at Re = 200000, the flow around the airfoil becomes more stable, and the moment coefficient stabilizes. Particularly high stability is observed at Re = 1000000, where the C_m curve remains virtually unchanged, indicating that maximum static stability has been achieved.

Sharp breaks and changes in slope on the C_m graph indicate the onset of flow separation. For Re = 50000–100000, separation occurs relatively early – at angles of attack $\alpha \approx 4$–6°, which reduces aerodynamic efficiency. However, at Re = 500000 and above, separation is delayed until $\alpha \approx 12$–14°, ensuring stable airfoil operation even under high loads.

It should be noted that the C_m values remain negative for all Reynolds numbers studied, indicating static stability. As the angle of attack increases, the aerodynamic moment decreases, ensuring stability and effective control of flight or turbine operation.

Overall, the S818 airfoil is designed for use in wind turbines and demonstrates best performance at Re ≥ 200000. Therefore, the airfoil is recommended for use in medium and high Reynolds number environments, where high aerodynamic efficiency and stability are ensured.

In aerodynamic optimization problems, the relationship between the lift coefficient (C_L) and drag coefficient (C_D) is of significant importance when $C_L/C_D \rightarrow$ maximum.

This value determines the aerodynamic quality of the profile and helps to determine the most advantageous angle of attack for efficient flight.

Fig. 14 shows the variation of the aerodynamic quality C_L/C_D with angle of attack α for the S818 airfoil, computed using the SST k-ω turbulence model. At small angles of attack (2–6°), C_L/C_D increases sharply – the maximum value (~52) is reached at $\alpha = 5°$, indicating the most efficient aerodynamic operation of the airfoil. After the peak, C_L/C_D decreases – at $\alpha = 8$–12°, efficiency drops significantly, associated with increased drag and possibly the onset of flow separation. At angles above 14°, C_L/C_D falls sharply – to a value of 5 at $\alpha = 18°$, indicating flow separation and a substantial increase in drag.

Thus, the S818 airfoil achieves optimal performance in the angle-of-attack range of 4° to 8°, especially at medium and high Reynolds numbers. This range should be considered when designing wind turbine blades to ensure maximum efficiency.

The S818-NR airfoil is primarily designed for small-scale wind turbines because it maintains efficient operation even at low wind speeds. In this research, its performance was analysed across a wide range of angles of attack to identify the most effective operating regimes. These results

provide essential data for the development of modern small-capacity wind turbines and for optimising their aerodynamic efficiency.

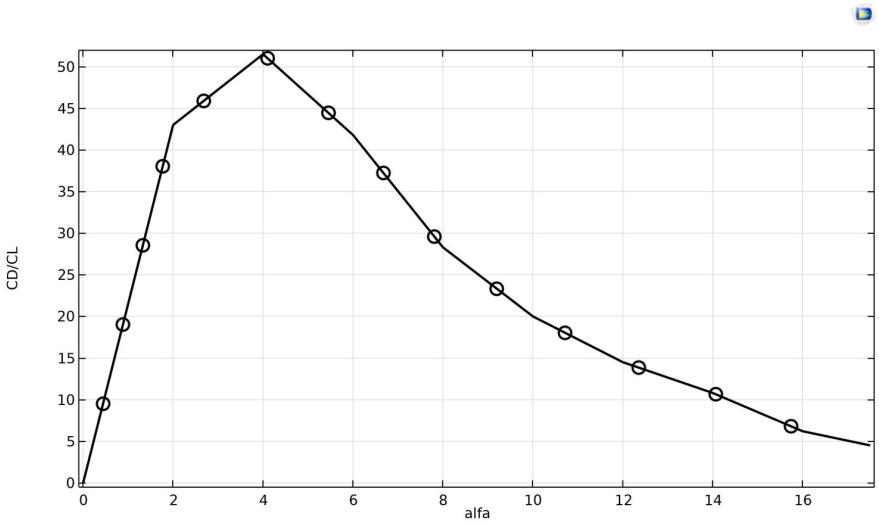


Fig. 14. Graph of aerodynamic quality C_L/C_D depending on the angle of attack α

The current research is limited to 2D numerical simulations, which may not fully capture 3D aerodynamic effects such as blade-tip vortices. To ensure reproducibility, standardised turbulence models and refined mesh configurations were used in COMSOL Multiphysics. Future research will involve 3D modelling to analyse the performance of full-scale wind turbine assemblies integrated with these airfoils.

4. Conclusion

The standard SST turbulence model is used to simulate the flow around the S818-NR airfoil. The results are presented in the article. *k-ω* is implemented in the Comsol Multiphysics software package, which uses the finite element method. Velocity fields, pressure coefficients, and other parameters are analysed.

The *SST k-ω* model adequately predicts both lift and drag for the S818 airfoil. The best agreement with experiment is observed at angles of attack up to 12–14°. The model can be effectively applied for numerical aerodynamic analysis of this airfoil in the range of moderate angles of attack.

The S818-NR airfoil provides engineers and designers with useful data. This data can be used to improve aerodynamic efficiency, optimise airfoil shape, and create more efficient wind turbines and aircraft. Understanding the airfoil's aerodynamic characteristics through numerical simulations aids the development of innovative technologies for renewable energy sources for industry.

The profile has low aerodynamic drag, which helps save fuel and increase aircraft speed. The profile is designed to minimise turbulence, which improves the stability and control of the aircraft.

S818-NR airfoil is a highly efficient solution for wind turbine blade design. Its geometric and aerodynamic properties provide high lift, low drag, and excellent lift-to-drag ratio, making it an ideal choice for modern wind turbines.

Conflict of interest

The authors declare that they have no conflict of interest in relation to this research, whether financial, personal, authorship or otherwise, that could affect the research and its results presented in this paper.

Financing

The research was performed without financial support.

Data availability

Data will be made available on reasonable request.

Use of artificial intelligence

The authors confirm that they did not use artificial intelligence technologies in creating the submitted work.

Acknowledgements

The authors would like to express their sincere gratitude to their colleagues for valuable guidance and insightful discussions throughout this research. Special thanks are extended to the Institute of Mechanics and Seismic Stability of Structures named after M. T. Urazbaev, Uzbekistan Academy of Sciences, for providing the necessary facilities and computational resources. This research was also financially supported by the same Institute, which funding made the successful completion of this work possible.

Authors' contributions

Hamdamov Muzaffar: Conceptualization, Ideas Author.

Muzaffarov Sardorbek: Formal Analysis, Application of statistical, mathematical, computational, or other formal techniques to analyze or synthesize research data.

Aminov Khayotjon: Investigation, Conducting a research and investigation process, specifically performing the experiments, or data/evidence collection.

Maratov Khushvaqt: Funding Acquisition, Acquisition of the financial support for the project leading to this publication.

References

[1] Fertahi, S. e.-D., Rehman, S., Benini, E., Lahrech, K., Samaouali, A., Arbaoui, A. et al. (2025). Insights from the Last Decade in Computational Fluid Dynamics (CFD) Design and Performance Enhancement of Darrieus Wind Turbines. Processes, 13 (2), 370. https://doi.org/10.3390/pr13020370

[2] Guerri, O., Bouhadef, K., Harhad, A. (2006). Turbulent Flow Simulation of the NREL S809 Airfoil. Wind Engineering, 30 (4), 287–301. https://doi.org/10.1260/030952406779295471

[3] Orozco Murillo, W., Palacio-Fernande, J. A., Patiño Arcila, I. D., Zapata Monsalve, J. S., Hincapié Isaza, J. A. (2020). Analysis of a Jet Pump Performance under Different Primary Nozzle Positions and Inlet Pressures using two Approaches: One Dimensional Analytical Model and Three Dimensional CFD Simulations. Journal of Applied and Computational Mechanics, 6, 1228–1244. https://doi.org/10.22055/JACM.2020.33339.2205

[4] Feng, J., Zhu, G., Lin, Y., Li, Y., Wu, G., Lu, J. (2020). Control of Dynamic Stall of an Airfoil by Using Synthetic Jet Technology. Arabian Journal for Science and Engineering, 45 (11), 9835–9841. https://doi.org/10.1007/s13369-020-04954-0

[5] Hadad, K., Eidi, H. R., Mokhtari, J. (2017). VOC level control by ventilation improvement of Flexography printing room using CFD modeling. Journal of Applied and Computational Mechanics, 3 (3), 171–177. https://doi.org/10.22055/jacm.2017.21452.1100

[6] Jaffar, H., Al-Sadawi, L., Khudair, A., Biedermann, T. (2024). Aerodynamic Characteristics Evaluation of S-Series Airfoils. Engineering and Technology Journal, 42 (1), 65–77. https://doi.org/10.30684/etj.2023.141757.1512

[7] Bertagnolio, F., Sørensen, N. N., Johansen, J., Fuglsang, P. (2001). Wind turbine airfoil catalogue. Forskningscenter Risoe. Available at: https://backend.orbit.dtu.dk/ws/files/7728949/ris_r_1280.pdf

[8] Guilmineau, E., Piquet, J., Queutey, P. (1997). Two-dimensional turbulent viscous flow simulation past airfoils at fixed incidence. Computers & Fluids, 26 (2), 135–162. https://doi.org/10.1016/s0045-7930(96)00034-5

[9] D Hu, D., Hua, O., Du, Z. (2006). A study on stall-delay for horizontal axis wind turbine. Renewable Energy, 31 (6), 821–836. https://doi.org/10.1016/j.renene.2005.05.002

[10] Chaviaropoulos, P. K., Hansen, M. O. L. (2000). Investigating Three-Dimensional and Rotational Effects on Wind Turbine Blades by Means of a Quasi-3D Navier-Stokes Solver. Journal of Fluids Engineering, 122 (2), 330–336. https://doi.org/10.1115/1.483261

[11] Fuglsang, P., Bak, C. (2004). Development of the Risø wind turbine airfoils. Wind Energy, 7 (2), 145–162. https://doi.org/10.1002/we.117

[12] Li, X., Yang, K., Zhang, L., Bai, J., Xu, J. (2014). Large thickness airfoils with high lift in the operating range of angle of attack. Journal of Renewable and Sustainable Energy, 6 (3). https://doi.org/10.1063/1.4878846

[13] Menter, F. R. (1994). Two-equation eddy-viscosity turbulence models for engineering applications. AIAA Journal, 32 (8), 1598–1605. https://doi.org/10.2514/3.12149

[14] Catalano, P., Amato, M. (2003). An evaluation of RANS turbulence modelling for aerodynamic applications. Aerospace Science and Technology, 7 (7), 493–509. https://doi.org/10.1016/s1270-9638(03)00061-0

[15] Tulapurkara, E. G. (1997). Turbulence models for the computation of flow past airplanes. Progress in Aerospace Sciences, 33 (1-2), 71–165. https://doi.org/10.1016/s0376-0421(96)00002-4

[16] Kral, L. D. (1998). Recent experience with different turbulence models applied to the calculation of flow over aircraft components. Progress in Aerospace Sciences, 34 (7-8), 481–541. https://doi.org/10.1016/s0376-0421(98)00009-8

[17] Du, Z., Selig, M. S. (2000). The effect of rotation on the boundary layer of a wind turbine blade. Renewable Energy, 20 (2), 167–181. https://doi.org/10.1016/s0960-1481(99)00109-3

[18] Sørensen, N. N., Michelsen, J. A. (2004). Drag Prediction for Blades at High Angle of Attack Using CFD. Journal of Solar Energy Engineering, 126 (4), 1011–1016. https://doi.org/10.1115/1.1807854

[19] Sørensen, N. N., Michelsen, J. A., Schreck, S. (2002). Navier–Stokes predictions of the NREL phase VI rotor in the NASA Ames 80 ft × 120 ft wind tunnel. Wind Energy, 5 (2-3), 151–169. https://doi.org/10.1002/we.64

[20] Ravshanov, S., Aminov, K., Rahmonova, N. (2025). Simulation of flow dynamics in a gas network pipe. 6th International Conference for Physics and Advance Computation Sciences: Icpas2024, 3282, 60007. https://doi.org/10.1063/5.0265131

[21] Turbulence Modeling Resource. NASA. Available at: http://turbmodels.larc.nasa.gov

[22] Hamdamov, M. M., Ishnazarov, A. I., Mamadaliev, K. A. (2023). Numerical Modeling of Vertical Axis Wind Turbines Using ANSYS Fluent Software. Internet of Things, Smart Spaces, and next Generation Networks and Systems, 156–170. https://doi.org/10.1007/978-3-031-30258-9_14

[23] Hamdamov, M., Muzaffarov, S. (2025). Simulation of turbulent flow around a thin rectangle using k-ε turbulence and environment models comsol multiphysics. 6th International Conference for Physics and Advance Computation Sciences: Icpas2024, 3282, 60013. https://doi.org/10.1063/5.0265168

[24] Hamdamov, M., Fayziev, R., Muzaffarov, S. (2024). Numerical simulation of wind turbines conducted using COMSOL software. E3S Web of Conferences, 541, 1001. https://doi.org/10.1051/e3sconf/202454101001

[25] Khujaev, I., Shirinov, Z., Ravshanov, S. (2025). Mathematical model and calculation algorithm modern heat exchanger connected to a two-pipe heating network. 6th International Conference for Physics and Advance Computation Sciences: Icpas2024, 3282, 60002. https://doi.org/10.1063/5.0267610

[26] Khojiqulov, S. (2025). Numerical method for solving pipeline transport equations of real fluid under given laws of change of pressure at inlet and mass flow at outlet of pipeline. 6th International Conference for Physics and Advance Computation Sciences: Icpas2024, 3282, 60004. https://doi.org/10.1063/5.0265139

[27] Bozorov, O. Sh., Khujaev, I., Aminov, Kh., Khojikulov, Sh. (2023). Application of fourier method to study propagation of compression shock wave in pipelines with damper. E3S Web of Conferences, 401, 1045. https://doi.org/10.1051/e3sconf/202340101045

Received 12.01.2026
Received in revised form 22.02.2026
Accepted 20.04.2026
Published 11.05.2026

© The Author(s) 2026
This is an open access article
under the Creative Commons CC BY license
https://creativecommons.org/licenses/by/4.0/

How to cite: *Hamdamov, M., Aminov, K., Muzaffarov, S., Maratov, K. (2026). Implementation of advanced turbulence models in aerodynamic performance prediction of the S818-NR airfoil. EUREKA: Physics and Engineering, 3, 15–33. https://doi.org/10.21303/2461-4262.2026.004263*